Геология и геофизика, 2017, т. 58, № 12, с. 1975—1994

УДК 550.8.01

ЗАКОНЫ СМЕШЕНИЯ И ПРИЧИННОСТЬ В ВЫСОКОЧАСТОТНЫХ ИНДУКЦИОННЫХ КАРОТАЖНЫХ ДИАГРАММАХ

Л. Табаровский, С. Форган

Baker Hughes, a GE Company, Houston Technology Center, 2001 Rankin Road, Houston, TX 77073, USA

Высокочастотные электромагнитные технологии для оценки приповерхностного пласта обеспечивают высокое пространственное разрешение и новые возможности для петрофизической интерпретации данных. Дисперсия свойств горных пород и переход от масштаба поры до масштаба коллектора (гомогенизация) представляют две наиболее сложные проблемы.

В электродинамике пористых сред используются различные законы смешения и дисперсии для гомогенизации свойств горных пород и описания их частотных характеристик. Законы смешения и дисперсия тесно связаны с основополагающим физическим принципом причинности и поэтому не могут быть введены произвольно. Для введения закона смешения/дисперсии необходимо доказать, что имеет место причинность. Для этого мы используем теорему Титчмарша и, в частности, одну из ее модификаций – соотношения Крамерса—Кронига. Причинность обсуждается для моделей Дебая, Коула-Коула, Хаврильяка—Негами и КМПВ. Дисперсия тесно связана с распространением волн. Оценка фазовых и групповых скоростей проливает свет на физику измерений фазы и амплитуды в поглощающей среде. Мы сделали оценку обеих скоростей и их зависимости от пространственных спектров или, другими словами, от расположения передающих и приемных элементов.

Чтобы проиллюстрировать теоретические выводы, мы приводим в качестве примера диэлектрический каротаж. Обычно в современных диэлектрических инструментах используются амплитудные и фазовые данные для различных частот и положений датчиков. Измеренная фаза дискретна на высоких частотах, и требуется обнаружение ее дискретности, так же как и развертывание. Примечательно, что можно определить затухание пласта и угол потерь исходя из многочастотных/мультисенсорных амплитудных данных и преобразовать их в диэлектрическую проницаемость, удельное сопротивление и истинную непрерывную фазу.

Преобразования инструментальных данных, используемых в этой статье, применимы для концептуального исследования и характерны для однородного пласта. Мы намеренно не учитываем точность измерений и распространение ошибок в процессе инверсии, поскольку они зависят от аппаратуры и способа обработки данных. При использовании различной аппаратуры требуются совместный анализ всех доступных данных и применение специальных методов шумоподавления, связанных со структурой системы сбора данных.

Электроразведка, диэлектрический каротаж, дисперсия, законы смешения, причинность.

MIXING LAWS AND CAUSALITY IN HIGH FREQUENCY INDUCTION LOG APPLICATIONS

L. Tabarovsky and S. Forgang

High frequency electromagnetic technologies for subsurface formation evaluation provide high spatial resolution and new opportunities for petrophysical interpretation of data. Dispersion of rock properties and upscaling from pore to reservoir scale (homogenization) represent the two most challenging problems.

In electrodynamics of porous media, various mixing and dispersion laws are used to homogenize rock properties and describe their frequency behavior. Mixing laws and dispersion have a close link to the fundamental physical principle of causality and therefore cannot be introduced arbitrarily. For any mixing/dispersion law, we need to prove that causality holds. For testing causality, we use *Titchmarsh's theorem* and, particularly, one of its modifications – *Kramers–Kronig relations*. Causality is discussed for *Debye, Cole–Cole, Havriliak–Negami, and CRIM* models.

Dispersion is closely related to wave propagation. Evaluation of phase and group velocities shed new light on the physics of phase and amplitude measurements in lossy media. We evaluated various definitions of both velocities and their dependence on spatial spectra or, in other words, on the arrangement of transmitting and receiving elements.

To illustrate theoretical findings, we use dielectric logging as an exemplary technology. Usually, in modern dielectric tools, amplitude and phase data are acquired, for various frequencies and sensor positions. The measured phase is discontinuous at high frequencies and requires detection of discontinuity as well as unwrapping. Remarkably, one can determine formation attenuation and loss angle based on multifrequency/multisensor amplitude data and transform them into dielectric permittivity, resistivity, and true continuous phase.

Transformations of exemplary tool data used in this paper are suitable for a conceptual study and are specific for a uniform formation. We intentionally do not address the accuracy of measurements and the propagation of errors in the inversion process, since they are tool- and processing-specific. Different tools require joint analysis of all available data and special noise reduction techniques associated with the structure of the acquisition system.

Electromagnetics, dielectric logging, dispersion, mixing laws, causality

---

✉e-mail: leonty.tabarovsky@bakerhughes.com

DOI: 10.15372/GiG20171210

INTRODUCTION

High frequency electromagnetic technologies for subsurface formation evaluation provide high spatial resolution and new opportunities for petrophysical interpretation of data. Dispersion of rock properties and up-scaling from pore to reservoir scale (homogenization) represent the two most challenging problems.

In electrodynamics of porous media, various mixing and dispersion laws are used to homogenize rock properties and describe their frequency behavior. Mixing laws and dispersion have a close link to the fundamental physical principle of causality and therefore cannot be introduced arbitrarily. For any mixing/dispersion law, we need to prove that causality holds. [Alu et al. 2011] discuss an example of causality violation in Maxwell-Garnett mixing law. For testing causality, we use *Titchmarsh's theorem* [Toll 1956, Titchmarsh 1926, Nordebo 2013] and, particularly, one of its modifications – *Kramers-Kronig relations*. Causality is discussed for *Debye, Cole-Cole, Havriliak-Negami, and CRIM* models.

Dispersion is closely related to wave propagation. Evaluation of phase and group velocities shed new light on the physics of phase and amplitude measurements in lossy media. We evaluated various definitions of both velocities and their dependence on spatial spectra or, in other words, on the arrangement of transmitting and receiving elements.

To illustrate theoretical findings, we use dielectric logging as an exemplary technology. Usually, in modern dielectric tools, amplitude and phase data are acquired, for various frequencies and sensor positions. The measured phase is discontinuous at high frequencies and requires detection of discontinuity as well as unwrapping [Abbas 2005]. Remarkably, one can determine formation attenuation and loss angle based on multi-frequency/multi-sensor amplitude data and transform them into dielectric permittivity, resistivity and true continuous phase.

Transformations of exemplary tool data used in this paper are suitable for a conceptual study and are specific for a uniform formation. We intentionally do not address accuracy of measurements and propagation of errors in the inversion process since they are tool and processing specific. Real tools require joint analysis of all available data and special noise reduction techniques associated with the structure of the acquisition system.

We start the paper with description of generic dielectric tool (Section 2) that is used in following discussion of phase & group velocities, spectra, mixing laws, and causality (Sections 3-5).

GENERIC TOOL

We consider a generic tool schematically shown in Fig. 1. On the left, three transmitters (magnetic dipoles), T_1, T_2, and T_3, generate EM field measured by the sensor, R. A reciprocal configuration is shown on the right.

Measurements and useful field transformations

Let us consider a signal generated by a single transmitter in a single receiver. The normalized magnetic field, $h_z = H_z / \left(M / 2\pi L^3\right)$, may be expressed in the following way (Kaufman and Keller, 1989):

$$h_z = e^{-kL}\left(1+kL\right)e^{i\omega t} \tag{1}$$

$$k^2 = -i\omega\mu\left(\sigma - i\omega\varepsilon\right) = -\omega^2\mu\varepsilon - i\omega\mu\sigma \tag{2}$$

Here, M, L – transmitter moment (A·m^2) and spacing (m), respectively; $\omega = 2\pi f$, where f is frequency (Hz); t – time; σ – formation conductivity (S/m); $\varepsilon = \varepsilon^* \cdot \varepsilon_0$ – formation dielectric permittivity (F/m); $\mu = \mu^* \cdot \mu_0$ – formation magnetic permeability (H/m); $\varepsilon_0 = 10^{-9}/(36\pi)$ F/m – dielectric permittivity of free space; $\mu_0 = 4\pi\times10^{-7}$ H/m – magnetic permeability of free space; ε^*, μ^* – permittivity and permeability relative to free space.

It follows from Eq. (2) that the complex number k^2 may belong only to the third quarter of a complex plane. Let us consider the following representation of k:

$$k = |k|e^{i\phi_k} = |k|\left(\cos\left(\varphi_k\right) + i\sin\left(\varphi_k\right)\right) \tag{3}$$

$$|k| = \sqrt{\omega\mu\sqrt{\left(\omega\varepsilon\right)^2 + \sigma^2}} \tag{4}$$

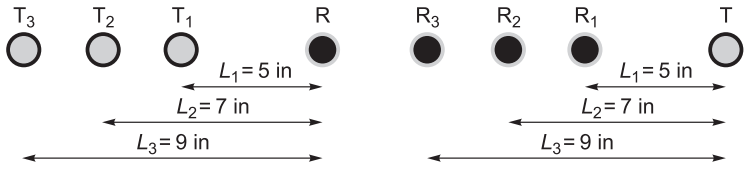

Fig. 1. Generic tool schematics.

$$\varphi_k = \frac{1}{2} a\tan 2(-\omega\mu, -\sigma) \tag{5}$$

$$-\pi/2 \le \varphi_k \le -\pi/4 \tag{6}$$

Here, atan2(x, y) means an argument of a complex number with real and imaginary parts equal x and y, respectively. Angle φ_k closely relates to the loss angle δ in formation: $\tan\delta = \tan(2\phi_k) = \sigma/\omega\varepsilon$.

We will need the following representation of the function (1 + kL) in Eq. (1):

$$(1+kL) = (1+|k|L*\cos(\phi_k)) + i(|k|L*\sin(\phi_k)) = |1+kL|e^{i\psi} \tag{7}$$

$$\begin{aligned} |1+kL| = A(L) &= \sqrt{(1+|k|L*\cos(\phi_k))^2 + (|k|L*\sin(\phi_k))^2} \\ &= \sqrt{1+2|k|L*\cos(\phi_k) + (|k|L)^2} \end{aligned} \tag{8}$$

$$\psi = \arctan\left(\frac{|k|L*\sin(\phi_k)}{1+|k|L*\cos(\phi_k)}\right), \quad \phi_k \le \psi \le 0, \quad |kL| \in (0,\infty) \tag{9}$$

Equations (1)-(9) result in the following expression for the normalized magnetic field, h_z:

$$h_z = A(L)e^{-\alpha - i\Phi}, \ \alpha = |k|L\cos(\phi_k), \ \Phi = |k|L\sin(\phi_k) - \psi + \omega t \tag{10}$$

Assuming $L_3 - L_2 = L_2 - L_1$ we introduce the following transformations of three magnetic fields produced by three transmitters in the receiver R:

$$D_2 = \frac{|h_z(L_3)|}{|h_z(L_2)|} = \frac{A(L_3)}{A(L_2)} e^{-|k|(L_3 - L_2)\cos(\phi_k)} \tag{11}$$

$$D_3 = \frac{|h_z(L_3)|}{|h_z(L_2)|}\frac{|h_z(L_1)|}{|h_z(L_2)|} - \frac{L_3 L_1}{(L_2)^2} = \frac{A(L_3)A(L_1)}{(A(L_2))^2} - \frac{L_3 L_1}{(L_2)^2} \tag{12}$$

Exemplary transformations (11) and (12) are useful for determining formation parameters, **σ** and **ε**. Other transformations may be considered as well. Please notice that $D_3 \to 0$ when $\omega \to \infty$. It provides increased sensitivity to formation parameters at high frequencies though requires improved accuracy of measurements.

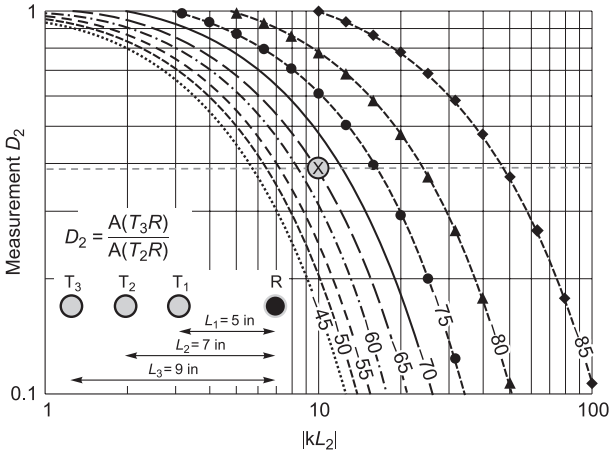

Fig. 2. Ratio of amplitudes, D_2 , as a function of parameter $|kL_2|$.

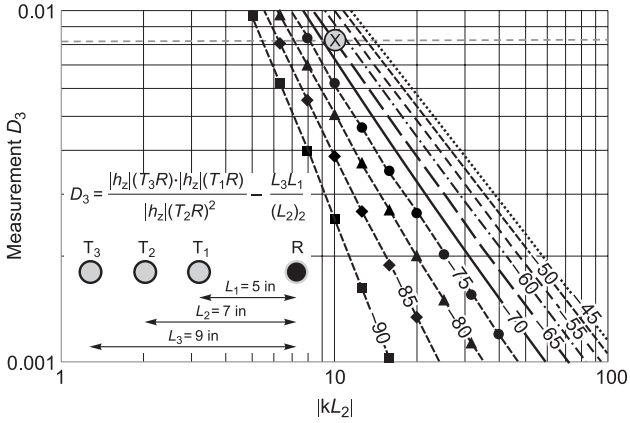

Fig. 3. Values of transformation, D_3 as a function of parameter $|kL_2|$.

Exemplary model and inversion

Given field transformations, D_2 and D_3, at a certain frequency, f, we can determine formation parameters, **σ** and **ε**. To illustrate the method, we selected the following model:

$$\boldsymbol{\sigma = 1.08\ S/m;\ \ \varepsilon = 55.62;\ \ f = 293311000\ Hz}$$

For the selected model, parameters $|kL_2|$ and ϕ_k have the following values (Eq. (4) and Eq. (5), Fig. 1):

$$|kL_2| = 10 \tag{13}$$

$$\varphi_k = -65° \tag{14}$$

For transformations D_2 and D_3 , Eq. (11) and Eq. (12) yield:

$$D_2 = 0.380 \tag{15}$$

$$D_3 = 0.008 \tag{16}$$

In Fig. 2 and Fig. 3, we describe functions $D_2(|kL_2|, \varphi_k)$ and $D_3(|kL_2|, \varphi_k)$.

Fig. 2 shows ratio of amplitudes, D_2, as a functions of parameter $|kL_2|$ (horizontal axis). Different curves correspond to different angles φ_k measured in degrees. The horizontal dashed line represents the exemplary value of $D_2 = 0.380$ in the exemplary model (Eq. 15). The crossed circle shows the exemplary model. Selecting crossings of curves with the dashed line we can determine a function $kL_2(\varphi_k)$. The function describes all feasible pairs of kL_2 and φ_k, for the given value of $D_2 = 0.380$. The function $kL_2(\varphi_k)$ is shown on Fig. 4 (square markers).

Similarly, fig. 3 shows values of transformation D_3, as a function of parameter $|kL_2|$ (horizontal axis). Different curves represent different angles φ_k measured in degrees. The horizontal dashed line, in this case, represents the exemplary value of $D_3 = 0.008$ for the exemplary model (Eq. 16). The crossed circle shows the exemplary model. Selecting crossings of curves with the dashed line we can determine a function $kL_2(\varphi_k)$. The function describes all feasible pairs of kL_2 and φ_k, for the given value of $D_3 = 0.008$. The function $kL_2(\varphi_k)$ is shown on Fig. 4 (triangular markers).

Fig. 4 provides summary of two step inversion.

Step 1. *Obtaining parameters $|kL_2|$ and φ_k from transformations D_2 and D_3.* Functions $kL_2\left(\varphi_k, D_2 = 0.380\right)$ (squares) and $kL_2\left(\varphi_k, D_3 = 0.008\right)$ (triangles) are monotonic, independent, and demonstrate quite good sensitivity to parameters. The point $|kL_2| = 10$, $\varphi_k = -65$ (exemplary model) is located in the crossing of both curves (please notice that the angle sign is reversed on the x-axis of the graph). The solution is unique.

Step 2. *Obtaining parameters **σ** and **ε** from $|kL_2|$ and φ_k.* Equations for reconstructing dielectric permittivity and conductivity are shown below the graphical solution for $|kL_2|$ and φ_k. The obtained values of **σ = 1.08 S/m** and **ε* = 55.6** correspond to exemplary model. Due to condition Eq. (6) the values of **σ** and **ε** are always positive.

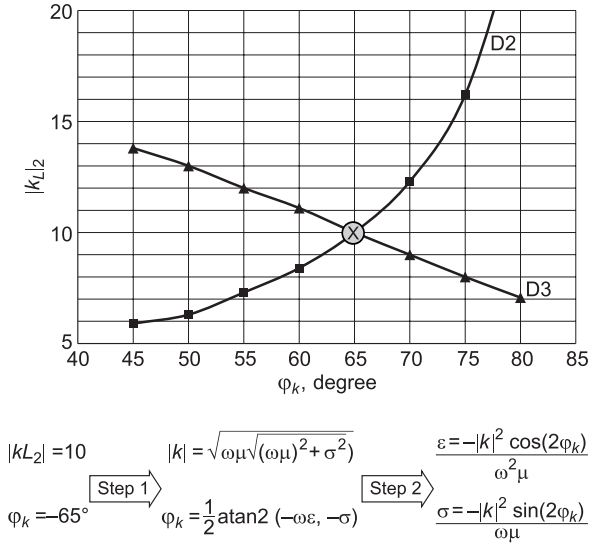

Fig. 4. Summary of inversion for exemplary model.

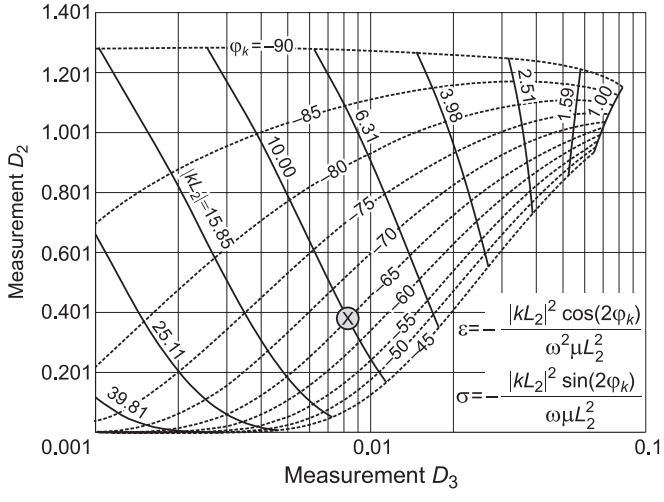

Fig. 5. Inversion chart for exemplary tool.

Inversion charts

In this section, an exemplary inversion chart is introduced (Fig 5). We intentionally illustrate inversion in a graphical form in order to provide an intuitive understanding of the physics. Of course, the algorithm can be implemented in a computer.

Inversion is performed in two steps:

Step 1. Two sets of curves in the plane D_3, D_2 represent constant values of parameters $|kL_2|$ (solid) and angle φ_k (dashed). Knowing from measurements the values of D_3 =0.008 (horizontal axis) and D_2 = 0.380 (vertical axis) we determine two curves crossing at the point (D_3, D_2): $|kL_2| = 10$ and $\varphi_k = -65°$.

Step 2. Equations for reconstructing dielectric permittivity and conductivity are shown in the right bottom corner of the graph. Since the values of ω, μ, and L_2 are known we obtain parameters of exemplary model: **σ = 1.08 S/m** and **ε* = 55.6**. The proposed approach may utilize phase measurements as well. Parameter $|kL_2|$ and loss angle resulting from amplitude inversion can be used for calculating the unwrapped phase (Eq. 9 & 10).

PHYSICS OF LOSS ANGLE: LINK TO PHASE VELOCITY

In this section, we will evaluate the dependence of formation phase velocity on the loss angle. The discussion is useful for understanding of phase measurement principles.

Key equations

Let us collect here, in one place, earlier derived equations relevant to the intended discussion. We will continue the previous sequential numbering of equations but will indicate the original equation numbers next to the new ones. Double numbering will be used only for the first appearance of already used equations. It will be helpful in finding derivations/discussions of the original equations.

Let us split Eq. (10):

$$h_z = A(L)e^{-\alpha - i\Phi} \tag{17/10}$$

$$\alpha = |k|L\cos(\varphi_k) \tag{18/10}$$

$$\Phi = |k|L\sin(\varphi_k) - \psi + \omega t \tag{19/10}$$

The phase ψ of pre-exponential factor $(1+kL)$ (see Eq. (1) for the field component h_z) has the following from:

$$\psi = \arctan\left(\frac{|k|L\cdot\sin(\varphi_k)}{1+|k|L\cdot\cos(\varphi_k)}\right), \quad \varphi_k \le \psi \le 0, \quad |kL| \in (0,\infty) \tag{20/9}$$

Let us consider expression for the wave number, |k|, Eq. (4):

$$|k| = \sqrt{\omega\mu\sqrt{(\omega\varepsilon)^2 + \sigma^2}} \tag{21/4}$$

Let us multiply Eq. (21) by $\sin(\varphi_k)$ and transform it to a physically more transparent form:

$$\begin{aligned} |k|\sin(\varphi_k) &= \sqrt{\omega^2\mu\varepsilon\sqrt{1+\left(\frac{\sigma}{\omega\varepsilon}\right)^2}}\,\sin(\varphi_k) = \\ &= \omega\sqrt{\mu_0\varepsilon_0}\,\sqrt{\mu^*\varepsilon^*}\sqrt[4]{1+\tan^2(2\varphi_k)}\sin(\varphi_k) = \frac{\omega}{c}\sqrt{\mu^*\varepsilon^*}\,\frac{\sin(\varphi_k)}{\sqrt{-\cos(2\varphi_k)}} \end{aligned} \tag{22}$$

Here, c — speed of light in free space.

Eq. (22) links the absolute value of wave number to the loss angle and the speed of light ***in formation***, $c/\sqrt{\mu^*\varepsilon^*}$.

Phase attributes

From Eq. (19), we observe that the phase φ is a function of distance, *L*, and time, *t*. The total differential of phase may be presented as follows:

$$d\Phi = \frac{\partial \Phi}{\partial L} dL + \frac{\partial \Phi}{\partial t} dt = \left(|k| \sin(\varphi_k) - \frac{\partial \psi}{\partial L} \right) dL + \omega dt \tag{23}$$

Analysis of Eq. (23) indicates that we can introduce three distinctly different phase characteristics:
Difference of phase values measured at two points at the same time. In this case, dt = 0 and

$$d\Phi = \left(|k| \sin(\varphi_k) - \frac{\partial \psi}{\partial L} \right) dL \tag{24}$$

Eq. (24) provides a definition of the phase gradient:

$$\frac{d\Phi}{dL} = \left(|k| \sin(\varphi_k) - \frac{\partial \psi}{\partial L} \right) \tag{25}$$

Difference of phase values measured at two times at the same point. In this case, $dL = 0$ and

$$d\Phi = \omega dt \tag{26}$$

Eq. (26) expresses the obvious fact: time derivative of phase equals to angular frequency.
Phase velocity. In this case, we choose certain value of phase and ride with this value in space and time. The following equation describes the movement:

$$d\Phi = 0 \tag{27}$$

Equations (27) and (23) yield:

$$\left(|k| \sin(\varphi_k) - \frac{\partial \psi}{\partial L} \right) dL + \omega dt = 0 \tag{28}$$

From Eq. (28) we obtain the expression for phase velocity, V_p:

$$\frac{dL}{dt} = V_p = -\frac{\omega}{|k| \sin(\varphi_k) - \frac{\partial \psi}{\partial L}} \tag{29}$$

Equations (25) and (29) lead to a remarkable connection of phase velocity and phase gradient:

$$\frac{\partial \Phi}{\partial L} = -\frac{\omega}{V_p} \tag{30}$$

In fact, the phase velocity and phase gradient are interchangeable.

Discussion of phase velocity

Detail derivation of phase velocity (Section 8) leads to the following equations:

$$V_p = \frac{V_p^0}{1 - \frac{1}{1 + 2|k|L \cdot \cos(\varphi_k) + (|k|L)^2}} \tag{31}$$

Here,

$$V_p^0 = -\frac{c}{\sqrt{\mu^* \varepsilon^*}} \frac{\sqrt{-\cos(2\varphi_k)}}{\sin(\varphi_k)} \tag{32}$$

At large distances, L → ∞ (far zone), the following holds (see Eq. (31)):

$$V_p \to V_p^0 \tag{33}$$

In this asymptotic limit, the phase velocity does not depend on the tool spacing and is determined exclusively by formation parameters and the frequency, see Fig. 6. Velocity in Fig. 6 is normalized by the speed of

light in formation. At the left end of horizontal axis (large conductivity and/or low frequencies), phase velocity tends to zero. It means that only standing wave exists under such conditions in the formation. At the right end of horizontal axis (small conductivity and/or high frequency), phase velocity tends to the speed of light in formation but never exceeds it.

At the opposite limit, $L \to 0$ (near zone), phase velocity tends to unlimitedly grow as follows from Eq. (31):

$$V_p \to \frac{V_p^0}{2|k|L \cdot \cos(\varphi_k)} \to \infty \tag{34}$$

Equation (34) is specific for the selected field component, h_z. It can be seen from Eq. (1) that in the near zone the linear dependence on the distance, L, disappears:

$$h_z = e^{-kL}(1 + kL)e^{i\omega t} \approx e^{-kL}e^{+kL}e^{i\omega t} \approx e^{i\omega t}$$

It means that the very definition of phase velocity (requiring the presence of a linear term with respect to distance) does not make sense in the near zone. Infinite phase velocity in the near zone, Eq. (34), is a consequence of this fact.

Over-luminal phase velocity does not contradict physics since it is not associated with propagation of energy. Indeed, the Pointing vector on the axis connecting transmitters and receivers equals to zero because electric field does not exist on this axis. It would be appropriate to study propagation of energy with all field components included. That would lead to a different behavior of phase. However, such study is beyond the scope of this paper.

Let us introduce the *Tool Factor* (or *α-factor*) as a ratio of phase velocity to its asymptotic value in far zone:

$$\alpha = \frac{V_p}{V_p^0} = \frac{1}{1 - \dfrac{1}{1 + 2|k|L \cdot \cos(\varphi_k) + (|k|L)^2}} \tag{35}$$

α – factor corrects asymptotic value of phase velocity to its actual value for the finite length of the tool:

$$V = \alpha V_p^0 \tag{36}$$

For L → ∞, Eq. (35) yields:

$$\alpha \to 1 \text{ (for } L \to \infty) \tag{37}$$

Fig.7 illustrates the behavior of α-factor in the near zone. In a large variety of spacings and loss angles, the phase velocity exceeds the speed of light in a

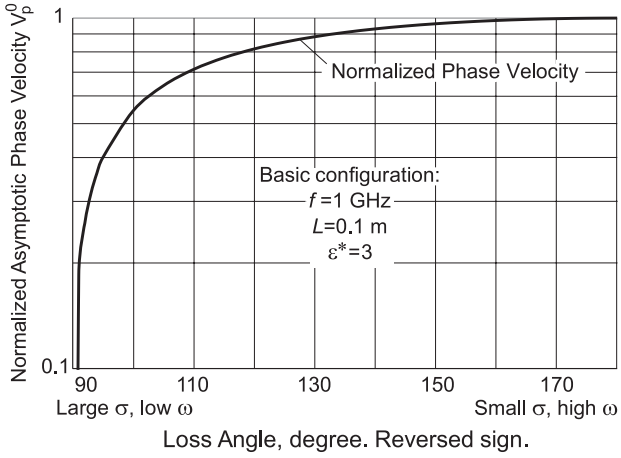

Fig. 6. Asymptotic phase velocity (in far zone) shown as a function of loss angle.

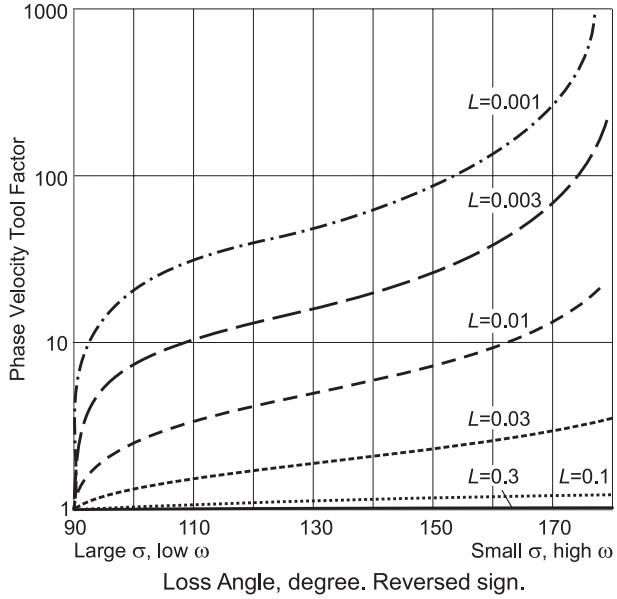

Fig. 7. α-factor in the near zone as a function of loss angle. The factor grows rapidly with the reduction of spacing L. Similar effect may be achieved by reducing frequency ω for a fixed value of spacing L.

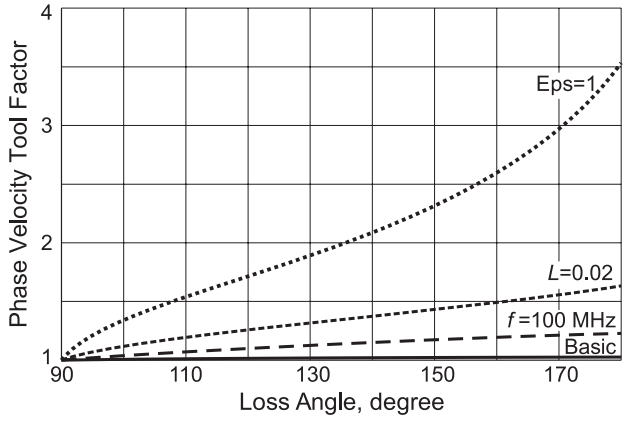

Fig. 8. α-factor for different tool parameters varying, one at a time, in basic tool configuration.

given formation. The factor grows rapidly with the reduction of spacing L. Similar effect may be achieved by reducing frequency ω for a fixed value of spacing L

Finally, in Fig. 8 we illustrate the behavior of α-factor while different tool parameters change (one at a time) in the selected basic tool configuration: $f = 1$ GHz, $L = 0.1$ m, $\varepsilon^* = 3$. Perturbed values of the perturbed parameters are indicated on the Fig. 8.

PHYSICS OF LOSS ANGLE: LINK TO GROUP VELOCITY

Group velocity is completely different from the phase velocity. It is related to evolution/propagation of a wave packet consisting of a group of spatial harmonics. As we will see, spatial harmonics in the wave packet have different velocity thus creating a condition for the packet dispersion (change of form) in the process of propagation.

In Attachment B, we consider spatially and temporally monochromatic waves. The spatial waves are monochromatic only in the plane perpendicular to the direction of propagation. They attenuate along the propagation path. Though spatial spectra are different for different field components F* they have a common analytic element affecting the wave propagation:

$$F^* \infty \exp(-pz - i\omega t) \tag{38}$$

Here,

$$p^2 = m^2 - i\omega\mu(\sigma - i\omega\varepsilon) = m^2 - \omega^2\mu\varepsilon - i\omega\mu\sigma \tag{39}$$

m – spatial wave number of Fourier transform.

For the wave velocity normalized by the speed of light in formation, V_g^n, we obtained the following expression (see Attachment B, Eq. (B13)):

$$V_g^n = \frac{1}{\frac{1}{2\sqrt{2}\sqrt{\sqrt{(y^2-1)^2+x^2}-(y^2-1)}}\left(\frac{-2(y^2-1)+x^2}{\sqrt{(y^2-1)^2+x^2}}+2\right)} \tag{40}$$

$$x = \frac{\sigma}{\omega\varepsilon}$$

$$y = \frac{\lambda}{\xi}$$

Here x is the tangent of the loss angle, λ is the light wavelength in the formation, ξ is the spatial wavelength.

Fig. 9 illustrates behavior of normalized group velocity as a function of formation loss angle. Different curves correspond to different ratios, y, of spatial and temporal wavelengths. Several observations need to be noted:

– It follows from Eq. B5, Attachment B, that propagation can occur only when $y \le 1$, i.e. when the spatial wavelength is greater than the electromagnetic wavelength in the formation. It is easy to understand by considering the limit of zero losses ($\sigma = 0$, $x = 0$) in Eq. B5. It should be $m^2 - \omega^2\mu\varepsilon < 0$ to maintain the square root as imaginary number. This condition is equivalent to the requirement of $y \le 1$.

– Losses do not affect propagation until tan(δ) approaches value of approximately 0.1.

– For small losses, reduction of spatial wavelength (or increase of y) results in reduction of the propagation velocity (see Fig. 9, compare different curves at tan(δ) <0.1).

– For large losses (tan(δ)>5), the wave propagation transforms into diffusion of current distribution, i.e. conduction effects take over propagation. The diffusion is the same for all spatial harmonics capable of propagating (see the right half of Fig. 9).

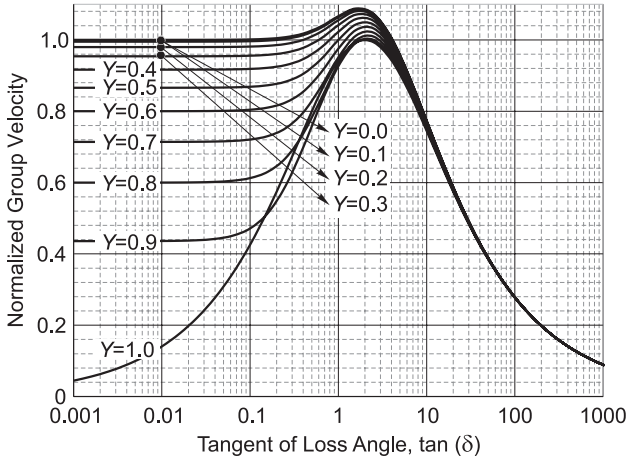

Fig. 9. Group velocity of spatial harmonics in a uniform formation. The velocity is normalized by the speed of light in formation. Different curves correspond to different values of y that is ratio of temporal and spatial wavelengths.

– In a transition zone, between propagation and diffusion, the group velocity may exceed the speed of light. It should not create a concern for two reasons: 1) for the diffusion limit ($x \to \infty$), the group velocity determined by Eq. (B12) or Eq. (B17), Attachment B, is twice phase velocity ($2\omega/(\mathrm{Im}(p))$) and may be arbitrarily large. For a correct estimation of group velocity in this case, it is necessary to consider movement of diffusion packets directly in time domain. Definition of group velocity as $d\omega/d\mathrm{Im}(p)$ used in Eq. (B12) is questionable in this case and requires further discussion.

– It is evident that a packet consisting of different spatial waves (having different values of y) will have evolving shape due to different velocity of constituent monochromatic waves.

SPECTRA, MIXING LAWS & CAUSALITY

We would like to address some issues related to dispersion and mixing laws used for data processing and inversion of dielectric measurements.

In electrodynamics of porous media, many mixing and dispersion laws are used. They have close link to the fundamental physical principle of causality and therefore cannot be introduced arbitrarily. Alu et al. [1] discuss an example of causality violation in Maxwell-Garnett mixing law. In other words, for any mixing/dispersion law (being used or being introduced) we need to check or prove that causality holds.

General discussion of causality

The causality principle claims (Toll [2]):

No output can occur before the input.

This simple statement translates to mathematical concepts of Convolution and Fourier transform resulting in strict criteria for causality.

Let us consider the direct and inverse Fourier transforms of a function $f(t)$ in the following form:

$$f^*(\omega) = \int_{=\infty}^{+\infty} f(t) e^{-i\omega t} d\omega \tag{41}$$

$$f(t) = \frac{1}{2\pi} \int_{=\infty}^{+\infty} f^*(\omega) e^{+i\omega t} d\omega \tag{42}$$

The sign convention in exponents, Eq. (41) and (42), is important for consistent consideration of causality. It is not the only one acceptable but it should be carefully followed, once chosen (Zvezdin et al., 1998).

If spectra of two functions, $f(t)$ and $g(t)$, are given the Convolution theorem imposes the following equivalent relations between $f(t)$, $g(t)$, and their spectra, $f^*(\omega)$ and $g^*(\omega)$:

$$\frac{1}{2\pi} \int_{-\infty}^{+\infty} f^*(\omega) g^*(\omega) e^{i\omega t} d\omega = \int_{-\infty}^{+\infty} f(t-\tau) g(\tau) d\tau \tag{43}$$

$$\frac{1}{2\pi} \int_{-\infty}^{+\infty} f^*(\omega) g^*(\omega) e^{i\omega t} d\omega = \int_{-\infty}^{+\infty} f(\tau) g(t-\tau) d\tau \tag{44}$$

Let us assume that

A. Input $f(t)$ starts at time $t = 0$ (requirement of action)

$$f(t) = 0 \text{ for } t < 0 \tag{45}$$

B. Future values of $f(t')$, $t' > t$ do not contribute to convolution (requirement of causality). This is equivalent to imposing condition

$$g(t) = 0 \text{ for } t < 0 \tag{46}$$

Requirements A and B result in the following:

1. For Equation (43):

a. Setting up to t the upper limit of integration variable τ (requirement A).

b. Setting up to 0 the low limit of integration. Otherwise, for negative values of τ, the output will depend on future values of $f(t)$ (requirement B).

2. For Equation (44):

c. Setting up to t the upper limit of integration variable τ. Otherwise, the output will depend on future values of $f(t)$ (requirement B).

d. Setting up to 0 the low limit of integration (requirement A).

Finally, the following is proven:

The Convolution theorem:

$$\int_{=\infty}^{+\infty} f^*(\omega)\, g^*(\omega) e^{i\omega t} d\omega = \int_0^t f(t-\tau)\, g(\tau) d\tau = \int_0^t f(\tau)\, g(t-\tau) d\tau \tag{47}$$

The causality condition (in time and frequency domain):

$$g(t) = 0 \text{ for } t < 0 \tag{48}$$

$$g^*(\omega) \text{ is analytical for } \mathrm{lm}(\omega) < 0 \tag{49}$$

If we want to ensure causality we need to ensure conditions (48) and (49).

Titchmarsh's theorem

Titchmarsh, in his famous theorem [Titchmarsh, 1926; Nordebo, 2013], suggested four equivalent formulations of causality (the first of which we already considered):

If a square integrable function $g^*(\omega)$ fulfills one of the four conditions below, then it fulfills all four of them:

1. The inverse Fourier transform $g(t)$ of $g^*(\omega)$ vanishes for $t < 0$, i.e.,

$$g(t) = 0 \text{ for } t < 0 \tag{50}$$

2. The function $g(\xi)$ is, for almost all ξ, the limit of an analytic function

$$f(\xi) = \lim_{v \to 0+} G(\xi + iv) \tag{51}$$

that is holomorphic in the upper half-plane and square integrable over any line parallel to the real axis:

$$\int_{-\infty}^{+\infty} \left| G(\xi + iv) \right|^2 d\xi < \infty \tag{52}$$

1. The functions Re $g^*(\omega)$ and lm $g^*(\omega)$ satisfy the first Plemelj formula

$$\mathrm{Re}\ g^*(\omega) = \frac{1}{\pi} P \int_{-\infty}^{+\infty} \frac{\mathrm{Re}\ g^*(\xi)}{\xi - \omega} d\xi \tag{53}$$

2. The functions Re $g^*(\omega)$ and lm $g^*(\omega)$ satisfy the second Plemelj formula

$$\mathrm{Im}\ g^*(\omega) = -\frac{1}{\pi} P \int_{-\infty}^{+\infty} \frac{\mathrm{Im}\ g^*(\xi)}{\xi - \omega}\, d\xi \tag{54}$$

Eq. (53) and (54) are known as Kramers-Kronig relations. P denotes the Cauchy principal value.

Application examples

One of the most practical ways of proving causality is checking condition (49) for the frequency dispersion of coefficients in constitutive equations. Let us consider dispersion of dielectric permittivity:

$$D(\omega)=\varepsilon(\omega)E(\omega) \tag{55}$$

Here, D – displacement field, ε – dielectric permittivity, E – electric field.

Assuming, in Eq. (47)-(49), $g^*(\omega)=\varepsilon(\omega)$ and $f^*(\omega)=E(\omega)$ we conclude that causality will follow from analyticity of ε(ω) in the low half-plane of complex ω.

In the following analysis, we consider causality of Debye, Cole-Cole, and Havriliak - Negami dispersion laws as well as CRIM mixing model for porous media.

Debye Relaxation

See for detail [Feldman et al., 2005], p.7.

$$\frac{\varepsilon(\omega)-\varepsilon_\infty}{\varepsilon_0-\varepsilon_\infty}=\frac{1}{1+(i\omega\tau)} \tag{56}$$

Here, ε_∞ – high-frequency permittivity limit, ε_0 – low frequency permittivity limit, τ – relaxsation parameter.

It is obvious that the right hand side of Eq. (56) has a single pole at $\omega=\frac{i}{\tau}$ thus being analytical in the lower half-plane of the complex ω.

Cole-Cole Relaxation

See for detail [Feldman et al., 2005], p. 8.

$$\frac{\varepsilon(\omega)-\varepsilon_\infty}{\varepsilon_0-\varepsilon_\infty}=\frac{1}{1+(i\omega\tau)^\alpha},\quad 0<\alpha<1 \tag{57}$$

Following [Van Gemert 1972] let us determine singularities in the right hand side of Eq. (57). We need to consider denominator and find it's zeros:

$$1+(i\omega\tau)^\alpha=1+|\omega\tau|e^{i\left(\frac{\pi}{2}+\varphi_\omega\right)\alpha} \tag{58}$$

Here φ_ω is the argument of a complex frequency ω.

It is evident that zeros are defined by the following equations:

$$|\omega\tau|=1 \tag{59}$$

$$\left(\frac{\pi}{2}+\varphi_\omega\right)\alpha=(2k+1)\pi,\quad k=0,\ \pm1,\ \pm2\ldots \tag{60}$$

Eq. (60) results in the following relation determining angular positions of singularities on the unit circle (59):

$$\varphi_\omega=\pi\left(\frac{1}{2}+\left(\frac{1}{\alpha}-1\right)+\frac{2k}{\alpha}\right),\quad k=0,\ \pm1,\ \pm2\ldots \tag{61}$$

Let us determine branch cut as follows:

$$-\frac{3}{2}\pi\le\varphi_\omega\le\frac{\pi}{2} \tag{62}$$

It is easy to see that no singularities, Eq. (61), falls on this branch thus proving that Cole-Cole relaxation function is analytical in the low complex half-plane.

Havriliak-Negami Relaxation

See for detail [Feldman et al., 2005]

$$\frac{\varepsilon(\omega)-\varepsilon_\infty}{\varepsilon_0-\varepsilon_\infty}=\frac{1}{\left(1+(i\omega\tau)^\alpha\right)^\beta},\quad 0<\alpha,\ \beta<1 \tag{63}$$

Selecting branch cut as in the case of Cole-Cole polarization we can notice that exponent β does not affect positions of singularities . Therefore, Havriliak-Negami relation maintains causality.

[Kalmykov et al. 2004] studied Havriliak-Negami relaxation in time domain. It is shown that the Debye rotational diffusion model of dielectric relaxation of polar molecules may be extended to yield the empirical Havriliak-Negami (HN) equation of anomalous dielectric relaxation from a microscopic model based on a kinetic equation just as in the Debye model. This kinetic equation is obtained by means of a generalization of the noninertial Fokker-Planck equation of conventional Brownian motion (generally known as the Smoluchowski equation) to fractional kinetics governed by the HN relaxation mechanism. For the simple case of noninteracting dipoles it may be solved by Fourier transform techniques to yield the Green function and the complex dielectric susceptibility corresponding to the HN anomalous relaxation mechanism. The HN relaxation in-time domain is described by Fox-Wright functions.

Complex Refractive Index Model (CRIM)

See for detail [Sabouroux and Ba, 2011], p. 5.

Complex Refractive Index Model (CRIM) is a mixing law used for approximation of dielectric permittivity of multi-component material mixtures, particularly, porous formations:

$$\varepsilon_{cri}^{\alpha} = (1-\Phi)\varepsilon_m^{\alpha} + S_w \Phi \varepsilon_w^{\alpha} + (1-S_w)\Phi \varepsilon_o^{\alpha} \qquad -1 \le \alpha \le 1 \tag{64}$$

Here, ε_{cri} – dielectric permittivity of rock mixture, ε_m – dielectric permittivity of rock matrix, ε_w – dielectric permittivity of water, ε_0 – dielectric permittivity of oil, Φ – porosity, S_w – water saturation.

In petrophysical applications, the most commonly used value of α is 0.5:

$$\varepsilon_{cri}^{0.5} = (1-\Phi)\varepsilon_m^{0.5} + S_w \Phi \varepsilon_w^{0.5} + (1-S_w)\Phi \varepsilon_o^{0.5} \tag{65}$$

We will use in our analysis more general expression for dielectric permittivity that includes Maxwell-Wagner polarization [Gibson et al. 2008]:

$$\varepsilon(\omega) = \varepsilon_\infty + \frac{\varepsilon_0 - \varepsilon_\infty}{\left(1 + (i\omega\tau)^{\alpha}\right)^{\beta}} + \frac{\sigma}{i\omega}, \quad 0 < \alpha < 1; \; 0 < \beta < 1 \tag{66}$$

To obtain expression for ε_{cri} we square both sides of Eq. (65):

$$\begin{gathered} \varepsilon_{cri} = (1-\Phi)^2 \varepsilon_m + S_w^2 \Phi^2 \varepsilon_w + (1-S_w)^2 \Phi^2 \varepsilon_o + \\ +2(1-\Phi) S_w \Phi \sqrt{\varepsilon_m \varepsilon_w} + 2(1-\Phi)(1-S_w)\Phi \sqrt{\varepsilon_m \varepsilon_o} + 2S_w \Phi (1-S_w)\Phi \sqrt{\varepsilon_w \varepsilon_o} \end{gathered} \tag{67}$$

The branching parts of the first three terms have the form of Havriliak-Negami dispersion and, consequently, are causal. For cross terms, it is not obvious. Let us consider, for example, the matrix-water term assuming, for simplicity, no dielectric dispersion:

$$\sqrt{\varepsilon_m \varepsilon_w} = \sqrt{\varepsilon_m}\sqrt{\varepsilon_w} = \sqrt{\varepsilon_m + \frac{\sigma_m}{i\omega}}\sqrt{\varepsilon_w + \frac{\sigma_w}{i\omega}}$$

Each square root has its own zero on the imaginary axis of frequency:

$$\omega_m = i\frac{\sigma_m}{\varepsilon_m} \tag{68}$$

$$\omega_w = i\frac{\sigma_w}{\varepsilon_w} \tag{69}$$

Since both branch points Eq. (68) and (69) are situated in the upper half-space they do not affect analyticity of the first three terms, eq. (67). It is also true for the remaining two cross-terms of Eq. (67).

Therefore, in the presence of only Maxwell-Wagner dispersion CRIM satisfies the causality conditions. More needs to be done to study CRIM when Debye, Cole-Cole, or Havriliak-Negami dispersion is present.

Maxwell-Garnett Mixing Formula with CRIM mixture in the background

In porous media, CRIM mixing law does not allow us to fit the data acquired by dielectric tool in a broad range of frequencies. Seleznev et al. [2006, 2011, 2014, 2015] suggested using Garnett-Maxwell mixing formula with CRIM model of porous formation (matrix, oil, and water) in the background.

$$\varepsilon_{eff} = \varepsilon_{cri} + \frac{\frac{1}{3}\sum_{j=1}^{n} f_j\left(\varepsilon_j - \varepsilon_{cri}\right)\sum_{i=1}^{3}\frac{\varepsilon_{cri}}{\varepsilon_{cri} + N_j^i\left(\varepsilon_j - \varepsilon_{cri}\right)}}{1 - \frac{1}{3}\sum_{j=1}^{n} f_j\left(\varepsilon_j - \varepsilon_{cri}\right)\sum_{i=1}^{3}\frac{N_j^i}{\varepsilon_{cri} + N_j^i\left(\varepsilon_j - \varepsilon_{cri}\right)}} \tag{70}$$

$$N_j^i = \int_0^\infty \frac{a_j^1 a_j^2 a_j^3}{\left(s + \left[a_j^i\right]^2\right)\sqrt{\left(s + \left[a_j^1\right]^2\right)\left(s + \left[a_j^2\right]^2\right)\left(s + \left[a_j^3\right]^2\right)}} ds \tag{71}$$

Here, n – number of inclusions (grains of ellipsoidal shape), ε_j – j-th inclusion complex permittivity, f_j – j-th inclusion volume fraction, N_j^i – i-th depolarization factor of j-th ellipsoid, a_j^1, a_j^2, a_j^3 – j-th ellipsoid semiaxes.

In further analysis, we will evaluate whether or not the effective dielectric permittivity, ε_{eff}, satisfies Kramers-Kronig relations. Evaluation of ε_{eff} analyticity in lower frequency half-space (Eq.(70)) will answer the question. For simplicity of analysis, we assume no dispersion. Therefore, Eq. (66) yields:

$$\varepsilon_j(\omega) = \varepsilon_{0,j} + \frac{\sigma_j}{i\omega} \tag{72}$$

The following equation should be solved in order to find zeros of denominator:

$$1 - \frac{f_1}{3}\sum_{i=1}^{3}\frac{N_1^i}{e_1 + N_1^i} - \frac{f_2}{3}\sum_{i=1}^{3}\frac{N_2^i}{e_2 + N_2^i} - \frac{f_3}{3}\sum_{i=1}^{3}\frac{N_3^i}{e_3 + N_3^i} = 0 \tag{73}$$

$$e_j = \frac{\varepsilon_{cri}}{\varepsilon_j - \varepsilon_{cri}} \tag{74}$$

Once poles e_j were found we can calculate from Eq. (74) the dielectric permittivity ε_j creating these poles:

$$\varepsilon_j = \left(\frac{1}{e_j} + 1\right)\varepsilon_{cri} \tag{75}$$

We can satisfy Eq. (73) by varying either of three parameters e_1, e_2, e_3 while keeping the remaining two intact. For example, resulting cubic equation for e_1 reads:

$$e_1^3\left[Q_1\right] + e_1^2\left[(Q_1 - 1)(x + y + z)\right] + e_1\left[(Q_1 - 2)(xy + yz + zx)\right] + \left[(Q_1 - 3)xyz\right] = 0$$

$$Q_1 = \frac{3}{f_1}\left[1 - \frac{f_2}{3}\sum_{i=1}^{3}\frac{N_2^i}{e_2 + N_2^i} - \frac{f_3}{3}\sum_{i=1}^{3}\frac{N_3^i}{e_3 + N_3^i}\right]$$

$$x = N_1^1, \quad y = N_1^2, \quad z = N_1^3$$

Similarly, we obtain for e_2 and e_3:

$$e_2^3\left[Q_2\right] + e_2^2\left[(Q_2 - 1)(x + y + z)\right] + e_2\left[(Q_2 - 2)(xy + yz + zx)\right] + \left[(Q_2 - 3)xyz\right] = 0$$

$$Q_2 = \frac{3}{f_2}\left[1 - \frac{f_1}{3}\sum_{i=1}^{3}\frac{N_1^i}{a_1 + N_1^i} - \frac{f_3}{3}\sum_{i=1}^{3}\frac{N_3^i}{a_3 + N_3^i}\right]$$

$$x = N_2^1, \; y = N_2^2, \; z = N_2^3$$

$$e_3^3\left[Q_3\right] + e_2^2\left[(Q_3 - 1)(x + y + z)\right] + e_2\left[(Q_3 - 2)(xy + yz + zx)\right] + \left[(Q_3 - 3)xyz\right] = 0$$

$$Q_3 = \frac{3}{f_2}\left[1 - \frac{f_1}{3}\sum_{i=1}^{3}\frac{N_1^i}{a_1 + N_1^i} - \frac{f_2}{3}\sum_{i=1}^{3}\frac{N_2^i}{a_2 + N_2^i}\right]$$

$$x = N_3^1, \; y = N_3^2, \; z = N_3^3$$

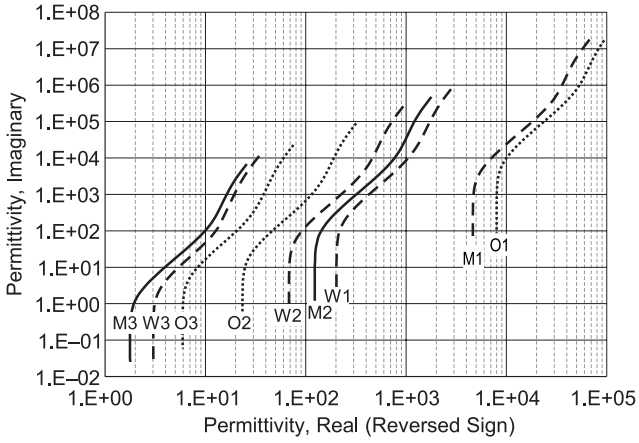

Fig. 10. Dielectric permittivities generated by poles for three component Maxwell-Garnett model.

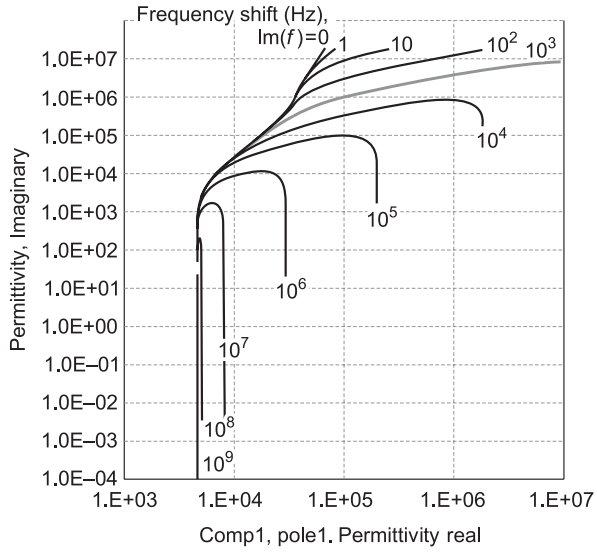

Fig. 11. Dielectric permittivities generated by the first pole of the first inclusion.

In Fig. 10, we show, as an example, the dielectric permittivities Eq. (75) corresponding to all the poles found for 37 frequencies within the range of 1 KHz to 1 GHz (total 333 cases). Each curve represents complex permittivities for 37 frequencies ranging from 1 KHz to 1 GHz. The lowest frequency always corresponds to the right upper end of each curve. Please notice that signs of real parts are reversed, for the convenience of graphical presentation. Therefore, all formation models generating poles have negative dielectric constants and are not feasible. It leads us to a conclusion that no poles exist on the real axis of frequency.

The below table describes the parameters used in modeling

INCLUSION PARAMETERS	HOST MEDIUM PARAMETERS
0.10E-05 Depolarization abs. error	0.30E+00 Porosity
0.10E-02 Depolarization rel. error	0.50E+00 Water saturation
0.10E+01 Comp.1 1st semiaxis	0.50E+01 Permitt. 1st phase (Matrix)
0.10E+02 Comp.1 2nd semiaxis	0.10E+01 Conduct. 1st phase (S/m)
0.10E+03 Comp.1 3rd semiaxis	0.60E+02 Permitt. 2nd phase (Water)
0.10E-04 Comp.1 conductivity, S/m	0.50E+01 Conduct. 2nd phase (S/m)
0.60E+01 Comp.1 rel. permittivity	0.10E+02 Permitt. 3d phase (Oil)
0.10E+01 Comp.2 1st semiaxis	0.10E-02 Conduct. 3d phase (S/m)
0.50E+01 Comp.2 2nd semiaxis	GRAIN VOLUME PARAMETERS
0.10E+02 Comp.2 3rd semiaxes	0.20E+00 Grain Volume (GrnVol)
0.10E+00 Comp.2 conductivity, S/m	0.70E+00 Comp.1 portion of GrnVol
0.80E+02 Comp.2 rel. permittivity	0.15E+00 Comp.2 portion of GrnVol
0.10E+01 Comp.3 1st semiaxes	0.15E+00 Comp.3 portion of GrnVol
0.20E+01 Comp.3 2nd semiaxes	DEPOLARIZATION FACTORS
0.70E+02 Comp.3 3rd semiaxes	N1 N2 N3
0.00E+00 Comp.3 conductivity, S/m	Comp.1 0.9075710E+00 0.8980450E-01 0.2611601E-02
0.50E+01 Comp.3 rel. permittivity	Comp.2 0.7994770E+00 0.1461682E+00 0.5435487E-01
	Comp.3 0.6659171E+00 0.3326445E+00 0.1444462E-02

Evaluation of poles along the frequency axis shifted to the lower complex half-plane brings similar results. We studied migration of poles when the frequency axis was shifted by 1, 10, 100, …, 10^8, 10^9 Hertz. The overall conclusion is that no poles exist in the low half-plane of frequency and, consequently, the Kramers-Kronig relation holds.

[Kolesnikova et al., 2004] studied causality of Maxwell-Garnett model in a wide band of frequencies by approximating Maxwell-Garnett mixing law by a series of Debye-like relaxation terms.

Fig. 11. Shows dielectric permittivities generated by the first pole of the first inclusion. Each curve represents complex permittivities for 37 frequencies ranging from 1 KHz to 1 GHz. The lowest frequency always corresponds to the right upper end of each curve. Curves differ by the frequency shift (measured in Hz) in the direction of the lower half-plane. Please notice that signs of real parts are reversed, for the convenience of graphical presentation. All shifts generate poles having negative dielectric constants. Therefore, they are not feasible. It leads us to a conclusion that no poles exist in the low half-plane of frequency and, consequently, the Kramers-Kronig relation holds.

SUMMARY

Application of various dispersion and mixing laws, that are mostly approximate or empirical, requires thorough evaluation of causality. We considered theoretical foundation of causality and suitable tests for high frequency logging applications. The main results are as follows:

– Causality confirmed analytically for Debye, Cole-Cole, Havriliak-Negami, and CRIM dispersion models;

– For Maxwell-Garnett mixing law with CRIM formation in the background, causality confirmed based on numerical evaluation of Kramers-Kronig relations;

– Closely related to causality and dispersion properties of phase and group velocities were studied for dielectric logging. Both velocities depend not only on the formation parameters but also on the transmitter-receiver configuration and position of sensors (far, near, or intermediate zone);

– Multi-coil/multi-frequency measurements of attenuation and loss angle allow for overcoming ambiguity of phase in high frequency well logging technologies.

REFERENCES

Abbas, K., 2005. A new recurrent approach for phase unwrapping. Int. J. Appl. Sci. Eng. 3 (2), 135–143.

Alu, A., Yaghjian, A.D., Shore, R.A., Silveirinha, M.G., 2011. Causality relations in the homogenization of metamaterials. Phys. Rev. 84, 054305.

Feldman, Y., Puzenko, A., Ryabov, Y., 2005. Dielectric relaxation fenomena in complex materials, in: Fractals, Diffusion, and Relaxation in Disordered Complex Systems. Advances in Chemical Physics, Part A, Vol. 133, pp. 1–125.

Gibson, N., Banks, H.T., Winfree, W.P., Smith, K., Chugh, N., 2008. Approximating Dispersive Mechanisms Using the Debye Model with Distributions of Dielectric Parameters. Oregon State University, Corvallis.

Kalmykov, Y.P., Coffey, W.T., Crothers, D.S.F, Titov, S.V., 2004. Microscopic models for dielectric relaxation in disordered systems. Phys. Rev. E 70, 041103.

Kaufman, A.A., Keller, G.V., 1989. Induction Logging. Elsevier Science Pub. Co. Inc., New York, NY.

Kolesnikova, M.Y., Wu, J., Zhang, J., Drewniak, J.L., Rozanov, K.N., 2004. Representation of permittivity for multiphase dielectric mixtures in FDTD modeling. Proc. IEEE Symp. Electromag. Compat., Vol. 1, 9–13.

Nordebo, S., 2013. Course 4FY826 Classical Electrodynamics, Lecture 7. Department of Physics and Electrical Engineering, Linnaeus University, Sweden.

Sabouroux, P., Ba, D., 2011. *EPSIMU*, A tool for dielectric properties measurement of porous media: Application in wet granular materials characterization. Progress in Electromagnetics Research B, Vol. 29.

Seleznev, N., Habashy, T., Boyd, A., Hizem, M., 2006. Formation properties derived from a multi-frequency dielectric measurement, in: SPWLA 47th Annual Logging Symposium, June 4–7, 2006.

Seleznev, N., Kleinberg, R.L., Herron, M.M., Machlus, M., Pomerantz, A.E., Reeder, S.L., Burnham, A.K., Day, R.L., Allix, P.C., 2011. Applications of dielectric dispersion logging to oil shale reservoirs, in: SPWLA 52nd Annual Logging Symposium, May 14–18, 2011, Paper O.

Seleznev, N., Fellah, K., Phillips, J., Zulkipli, S.N., Fournie, B., 2014. Matrix Permittivity Measurements for Rock Powders. SPE-170896-MS.

Seleznev, N., Fellah, K., Fournie, B., 2015. Method and Apparatus for Determining Permittivity of Rock Matrix. Pub. No: US 2015/0212228 A1, Jul. 30.

Titchmarsh, E.C., 1926. The zeros of certain integral functions. Proc. London Math. Soc. s2–25 (1), 283–302.

Toll, J.S., 1956. Causality and the dispersion relation: Logical foundations. Phys. Rev., Vol. 104, Issue 6, December 15.

Van Gemert, M.J.C., 1972. A note on the Cole–Cole dielectric permittivity equation in connection with causality. Chem. Phys. Lett. 14 (5), 606–608.

Zvezdin, A.K, Kotov, V.A., 1998. Modern Magnetooptics and Magnetooptical Materials. Taylor & Francis Group, NY.

ATTACHMENT A. DERIVATION OF PHASE VELOCITY

Let us consider Eq. (29), (20), and (22) (numbered here as (A1), (A2), and (A3), respectively):

$$\frac{dL}{dt} = -\frac{\omega}{|k|\sin(\varphi_k) - \frac{\partial \psi}{\partial L}} \tag{A1}$$

$$\psi = \arctan\left(\frac{|k|L \cdot \sin(\varphi_k)}{1 + |k|L \cdot \cos(\varphi_k)}\right), \quad \varphi_k \le \psi \le 0, \quad |kL| \in (0, \infty) \tag{A2}$$

$$|k|\sin(\varphi_k) = \frac{\omega}{c}\sqrt{\mu^* \varepsilon^*}\,\frac{\sin(\varphi_k)}{\sqrt{-\cos(2\varphi_k)}} \tag{A3}$$

Let us calculate the second term in denominator of Eq. (A1):

$$\begin{aligned}\frac{\partial \psi}{\partial L} = \frac{\partial \psi}{\partial kL}\frac{\partial kL}{\partial L} &= \frac{1}{1 + \left(\frac{|k|L \cdot \sin(\varphi_k)}{1 + |k|L \cdot \cos(\varphi_k)}\right)^2}\,\frac{\sin(\varphi_k)\left(1 + |k|L \cdot \cos(\varphi_k)\right) - |k|L \cdot \sin(\varphi_k)\cos(\varphi_k)}{\left(1 + |k|L \cdot \cos(\varphi_k)\right)^2}\,k \\ &= \frac{k\sin(\varphi_k)}{\left(1 + |k|L \cdot \cos(\varphi_k)\right)^2 + \left(|k|L \cdot \sin(\varphi_k)\right)^2} = \frac{k\sin(\varphi_k)}{1 + 2|k|L \cdot \cos(\varphi_k) + \left(|k|L\right)^2}\end{aligned} \tag{A4}$$

We obtain from Eq. (A1), Eq. (A4), and Eq. (A3):

$$\begin{aligned}\frac{dL}{dt} &= -\frac{\omega}{k\sin(\varphi_k)\left(1 - \frac{1}{1 + 2|k|L \cdot \cos(\varphi_k) + \left(|k|L\right)^2}\right)} = -\frac{\omega}{k\sin(\varphi_k)}\,\frac{1}{\left(1 - \frac{1}{1 + 2|k|L \cdot \cos(\varphi_k) + \left(|k|L\right)^2}\right)} \\ &= -\frac{c}{\sqrt{\mu^* \varepsilon^*}}\,\frac{\sqrt{-\cos(2\varphi_k)}}{\sin(\varphi_k)\left(1 - \frac{1}{1 + 2|k|L \cdot \cos(\varphi_k) + \left(|k|L\right)^2}\right)} \\ &= -\frac{c}{\sqrt{\mu^* \varepsilon^*}}\,\frac{\sqrt{-\cos(2\varphi_k)}}{\sin(\varphi_k)}\,\frac{1}{1 - \frac{1}{1 + 2|k|L \cdot \cos(\varphi_k) + \left(|k|L\right)^2}}\end{aligned} \tag{A5}$$

Finally:

$$V_p = \frac{V_p^0}{1 - \frac{1}{1 + 2|k|L \cdot \cos(\phi_k) + \left(|k|L\right)^2}} \tag{A6}$$

$$V_p^0 = -\frac{c}{\sqrt{\mu^* \varepsilon^*}}\,\frac{\sqrt{-\cos(2\varphi_k)}}{\sin(\varphi_k)} \tag{A7}$$

ATTACHMENT B. DERIVATION OF GROUP VELOCITY

Let us consider the expression describing propagation of spatial harmonics H_z^* in lossy medium:

$$H_z^* \propto \exp\left(-pz - i\omega t\right) \tag{B1}$$

Here,

$$p^2 = m^2 - i\omega\mu\left(\sigma - i\omega\varepsilon\right) = m^2 - \omega^2\mu\varepsilon - i\omega\mu\sigma \tag{B2}$$

m – spatial wave number in integral representation of H_z field component.

Equation (B1) includes the only part of H_z^* Fourier transform that is responsible for propagation of spatial harmonics.

Let us introduce real and imaginary part of p in Eq. B1:

$$H_z^* \propto \exp\left(-\mathrm{Re}\left(p\right)z\right)\exp\left(-i\left(\mathrm{Im}\left(p\right)z + \omega t\right)\right) \tag{B3}$$

According to definition of group velocity, V_g, we obtain:

$$V_g = \frac{z}{t} = -\frac{d\omega}{d\,\mathrm{Im}\left(p\right)} = -\frac{1}{\dfrac{d\,\mathrm{Im}\left(p\right)}{d\omega}} \tag{B4}$$

Let us calculate Im(p):

$$p = \sqrt{m^2 - \omega^2\mu\varepsilon - i\omega\mu\sigma} = a + ib \tag{B5}$$

$$a = m^2 - \omega^2\mu\varepsilon \tag{B6}$$

$$b = -\omega\mu\sigma \tag{B7}$$

According to well known formula:

$$p = \sqrt{a + ib} = \sqrt{\frac{\sqrt{a^2 + b^2} + a}{2}} + i\,\mathrm{sgn}\left(b\right)\sqrt{\frac{\sqrt{a^2 + b^2} - a}{2}} \tag{B8}$$

Using Eq. (B6), (B7), and B(8) yields:

$$\mathrm{Im}\left(p\right) = -\sqrt{\frac{\sqrt{a^2 + b^2} - a}{2}} = -\sqrt{\frac{\sqrt{\left(m^2 - \omega^2\mu\varepsilon\right)^2 + \omega^2\mu^2\sigma^2} - \left(m^2 - \omega^2\mu\varepsilon\right)}{2}} \tag{B9}$$

Series of exhausting but obvious calculations leads us to the expression for the group velocity:

$$\sqrt{2}\,\frac{d\,\mathrm{Im}\left(k\right)}{d\omega} = -\frac{1}{2\sqrt{\sqrt{\left(m^2 - \omega^2\mu\varepsilon\right)^2 + \omega^2\mu^2\sigma^2} - \left(m^2 - \omega^2\mu\varepsilon\right)}}\left(\frac{2\left(m^2 - \omega^2\mu\varepsilon\right)\left(-2\omega\mu\varepsilon\right) + 2\omega\mu^2\sigma^2}{2\sqrt{\left(m^2 - \omega^2\mu\varepsilon\right)^2 + \omega^2\mu^2\sigma^2}} + 2\omega\mu\varepsilon\right)$$

$$\sqrt{2}\,\frac{d\,\mathrm{Im}\left(p\right)}{d\omega} = -\frac{1}{\omega\sqrt{\mu\varepsilon}}\,\frac{1}{2\sqrt{\sqrt{\left(y^2 - 1\right)^2 + x^2} - \left(y^2 - 1\right)}}\left(\frac{\omega^2\mu\varepsilon\left(y^2 - 1\right)\left(-2\omega\mu\varepsilon\right) + \omega\mu^2\sigma^2}{\omega^2\mu\varepsilon\sqrt{\left(y^2 - 1\right)^2 + x^2}} + 2\omega\mu\varepsilon\right)$$

$$\sqrt{2}\,\frac{d\,\mathrm{Im}\left(p\right)}{d\omega} = -\frac{1}{\omega\sqrt{\mu\varepsilon}}\,\frac{\left(\omega^2\mu\varepsilon\right)\left(\omega\mu\varepsilon\right)}{2\sqrt{\sqrt{\left(y^2 - 1\right)^2 + x^2} - \left(y^2 - 1\right)}}\left(\frac{-2\left(y^2 - 1\right) + x^2}{\omega^2\mu\varepsilon\sqrt{\left(y^2 - 1\right)^2 + x^2}} + \frac{2}{\omega^2\mu\varepsilon}\right)$$

$$\frac{d\,\mathrm{Im}\left(p\right)}{d\omega} = -\frac{\sqrt{\mu\varepsilon}}{2\sqrt{2}\sqrt{\sqrt{\left(y^2 - 1\right)^2 + x^2} - \left(y^2 - 1\right)}}\left(\frac{-2\left(y^2 - 1\right) + x^2}{\sqrt{\left(y^2 - 1\right)^2 + x^2}} + 2\right)$$

$$y = \frac{m}{\omega\sqrt{\mu\varepsilon}} \tag{B10}$$

$$x = \frac{\sigma}{\omega\varepsilon} \tag{B11}$$

$$V_g = -\frac{d\omega}{d\,\mathrm{Im}(p)} = \frac{c}{\sqrt{\mu^*\varepsilon^*}} \frac{1}{\frac{1}{2\sqrt{2}\sqrt{\sqrt{\left(y^2-1\right)^2+x^2}-\left(y^2-1\right)}}\left(\frac{-2\left(y^2-1\right)+x^2}{\sqrt{\left(y^2-1\right)^2+x^2}}+2\right)} \tag{B12}$$

Introducing normalized group velocity, V_g^n, we obtain:

$$V_g^n = \frac{V_g}{c^*} = \frac{1}{\frac{1}{2\sqrt{2}\sqrt{\sqrt{\left(y^2-1\right)^2+x^2}-\left(y^2-1\right)}}\left(\frac{-2\left(y^2-1\right)+x^2}{\sqrt{\left(y^2-1\right)^2+x^2}}+2\right)} \tag{B13}$$

Here, x is the tangent of loss angle. The physical meaning of y becomes clear after following simple transformations of Eq. (B10):

$$y = \frac{m}{\omega\sqrt{\mu\varepsilon}} = \frac{mc^*}{2\pi f} = \frac{m}{2\pi}\frac{c^*}{f} = \frac{\lambda}{\xi} \tag{B14}$$

Here λ is the light wavelength in the formation, and ξ is the spatial wavelength corresponding to the spatial harmonic, m.

Let us present square root in Eq. (B5) as a function of parameters x and y:

$$p = \sqrt{m^2 - \omega^2\mu\varepsilon - i\omega\mu\sigma} = \omega\sqrt{\mu\varepsilon}\sqrt{\left(y^2-1\right)-ix} = \omega\frac{\sqrt{\mu^*\varepsilon^*}}{c}\sqrt{\left(y^2-1\right)-ix} \tag{B15}$$

$$\frac{dp}{d\omega} = \omega\frac{\sqrt{\mu^*\varepsilon^*}}{c}\frac{2y\left(-\frac{y}{\omega}\right)-i\left(-\frac{x}{\omega}\right)}{2\sqrt{\left(y^2-1\right)-ix}} == \frac{\sqrt{\mu^*\varepsilon^*}}{c}\left(\sqrt{\left(y^2-1\right)-ix}-\frac{2y^2-ix}{2\sqrt{\left(y^2-1\right)-ix}}\right) \tag{B16}$$

From Eq. (B16) and definition of group velocity Eq. (B12) we obtain:

$$V_g = \frac{d\omega}{d\,\mathrm{Im}(p)} = \frac{c}{\sqrt{\mu^*\varepsilon^*}} \frac{1}{\mathrm{Im}\left(\sqrt{\left(y^2-1\right)-ix}-\frac{2y^2-ix}{2\sqrt{\left(y^2-1\right)-ix}}\right)} \tag{B(17)}$$

Eq. B(17) is equivalent to Eq. (B12).

Рекомендована к печати 2 августа 2017 г.
М.И. Эповым

Поступила в редакцию
1 декабря 2016 г.